Nuclear Instruments and Methods in Physics Research A 1069 (2024) 169912

Contents lists available at ScienceDirect

Nuclear Inst. and Methods in Physics Research, A

journal homepage: www.elsevier.com/locate/nima

Full Length Article

High power target for the High Brilliance Neutron Source

J. Baggemann [a],*, T. Gutberlet [a], P. Zakalek [a], J. Wolters [b], U. Rücker [a], E. Mauerhofer [a], J. Li [a], Q. Ding [a], Th. Loewenhoff [c], D. Dorow-Gerspach [c], Y. Bessler [b], Th. Brückel [a]

[a] JCNS-HBS, Forschungszentrum Jülich, Wilhelm-Johnen-Weg, 52428, Jülich, Germany
[b] ZEA-1, Forschungszentrum Jülich, Wilhelm-Johnen-Weg, 52428, Jülich, Germany
[c] IEK-4, Forschungszentrum Jülich, Wilhelm-Johnen-Weg, 52428, Jülich, Germany

ARTICLE INFO

Keywords:
HiCANS
High power
Neutron target
HBS

ABSTRACT

The High Brilliance Neutron Source (HBS) is a High-Current Accelerator-driven Neutron Source (HiCANS) under development at Jülich Centre for Neutron Science - Forschungszentrum Jülich. The unique specifications of the HBS require a neutron target with a high neutron emission able to operate in vacuum with a 70 MeV proton beam with 90 mA peak current and 1.6% duty cycle leading to an average thermal load of 100 kW. A tantalum target of 100 cm^2 irradiated area with an internal cooling structure which removes the heat quite homogeneously, provides a good compromise between low pressure and high heat transfer and ensures an homogeneous protons energy loss was designed and optimized by means of MCNP, CFD and FEM simulations. Such a target was successfully manufactured and its operational capability was demonstrated by operating it under a heat load of 1 $\mathrm{kW\,cm^{-2}}$ from an electron gun.

1. Introduction

In the last few decades, proton accelerator-based neutron sources have emerged as useful alternatives to research reactors for scientific and industrial neutron beam research using cold, thermal and fast neutrons. Basically, existing accelerator-based neutron sources can be divided into two classes: (i) spallation neutron sources where neutrons are released via spallation processes by bombarding a target with protons at energies in the several 100 MeV to several GeV range, (ii) CANS (Compact Accelerator-driven Neutron Sources) where neutrons are emitted via nuclear reactions such as (p,xn) at energies of a few MeV and currents of a few μA. In recent years, a new type of accelerator-driven facility has emerged, currently only in the form of projects. These facilities are intended to bridge the gap between the high power spallation sources and the low power CANS. These so-called High-Current Accelerator-driven Neutron Sources (HiCANS) use similar reactions as CANS, but at higher beam energies up to 100 MeV and higher currents up to 100 mA in peak. They are designed to maximize beam brightness and to offer performance of their beamline instrumentation highly competitive with existing research reactors. In accelerator-based neutron sources the nuclear reactions happen in custom-build targets, designed and engineered to maximize the neutron yield and to ensure stable and safe operation. Table 1 shows an overview of targets, energies and power levels at selected sources.

Spallation targets consist of materials with a high atomic number Z such as lead, tantalum, tungsten or mercury. The proton beam illuminates the target over an area of between 100 cm^2 and 400 cm^2 with a depth of several tenth of centimetres. These targets have in common that they are designed to dissipate a high thermal load.

CANS targets use often low-Z materials such as beryllium or lithium, which have a higher neutron yield at proton energies below approx. 20 MeV in comparison to high-Z elements. The targets are usually less than a millimetre thick and their illuminated area is an order of magnitude smaller compared to spallation targets. Each set of accelerator parameters requires a dedicated target solution however in particular all targets face two specific issues which need to be solved: the risk of material blistering due to hydrogen implantation and high local heat loads due to the small thickness of the target.

The targets can be divided into three types: (i) stationary solid targets, (ii) rotating solid targets and (iii) liquid targets. From a technical point of view, stationary solid targets are the least complex and require the least installation space but limit the heat load. Rotating solid targets allow for higher heat deposition by reducing the average heat load by distributing the proton beam over several sub-targets or a larger target area. Rotating targets are large, complex and hence involve potential risks of operational failure. Liquid targets reduce the average heat load, the risk of blistering and of material stress, but they

---

* Corresponding author.
E-mail address: j.baggemann@fz-juelich.de (J. Baggemann).

https://doi.org/10.1016/j.nima.2024.169912
Received 31 July 2024; Received in revised form 12 September 2024; Accepted 21 September 2024

Table 1
Overview of neutron targets operated with proton beam at spallation sources, CANS and HiCANS.

	Facility	Power [kW]	Energy [MeV]	Current[a] [mA]	Material[b]	Type[c]	
Spallation	SINQ	950	575	1.6	Pb (25 kg)	solid	[1,2]
	ISIS TS-1	180	800	0.2	W-Ta (53 kg)	solid	[3]
	CSNS (T-1)	100	1600	0.06	W-Ta (45 kg)	solid	[4,5]
	LANSCE	80	800	0.1	W-Ta (57 kg)	solid	[6,7]
	ESS	5000	2000	2.5	W (3 t)	rotat.	[8]
	SNS	1200	1000	1.2	Hg (21.5 t)	liquid	[9,10]
	J-PARC	1000	3000	0.33	Hg (20 t)	liquid	[11]
CANS	LENS	3	13	0.23	Be (7 g)	solid	[12]
	RANS	0.7	7	0.1	Be (5.3 g)	solid	[13]
	RANS II	0.1	2.49	0.040	Li (40 mg)	solid	[14]
HiCANS	SARAF I	5	4	2	In	liquid	[15]
	SARAF II	200	40	5	GaIn	liquid	[16,17]
	ICONE[d]	50	20	2	Be	solid	[18]
	ARGITU[d]	45	31.5	1.44	Be	solid	[19]
	HBS[d]	100	70	1.43	Ta (4.4 kg)	solid	[20]

[a] time averaged proton current.

[b] limited to the neutron-producing material.

[c] “solid”: stationary solid target, “rotat.”: rotation solid target, “liquid”: liquid metal target.

[d] in development.

are complex systems due to the operation of liquid metal circuits. They also face high pulse pressures in the liquid, which increase the potential for cavitation damage.

Spallation sources are large scale facilities and offer high neutron yield due to the spallation process. CANS have been more applied as laboratory-based sources due to their lower technical complexity, lower regulatory requirements and lower neutron yields. HiCANS projects aim to push the thermal power at the target towards the technical feasible limit while keeping the proton beam energy below the spallation threshold. The aim is to design powerful neutron facilities with a competitive neutron flux at the sample. Optimized target-moderator-reflector systems and measures to optimize the neutron transport are used to compensate for the initial lower neutron yield.

Within the HBS (High Brilliance neutron Source) project, the Jülich Centre for neutron Science (JCNS) at Forschungszentrum Jülich has developed a new kind of HiCANS which shall serve as a competitive user facility. The technical design of the HBS is given in [20]. The HBS is driven by a 90 mA pulsed proton accelerator with a energy of 70 MeV and 1.6% duty cycle and with various pulses of 24 Hz and 96 Hz at the individual target stations. The peak power of 6 MW generates an average power of 100 kW per target station. For these requirements a new target was designed since neither the adaption of a spallation target was possible due to the different ion energy level nor the adaption of a CANS targets due to the much higher heat load on a HiCANS target. The development of this target design, its realization and testing are described in the following.

2. Target design

The three main guiding principles of the development of the HBS target are (i) to maximize the neutron emission, (ii) to feed optimally the cold and thermal moderators and (iii) to design a compact and reliable target. The neutron yield scales linearly with the thermal power at the target and increases with increasing ion energy [21]. Therefore, the target must be able to withstand the maximum thermal load. The selected proton energy is a compromise between neutron yield, shielding effort and accelerator costs. The size of the target depends in a first approximation on the dimensions of the cold moderator. The length of the cold moderator is about 10 cm corresponding to the free path length of cold neutrons in liquid para hydrogen. Therefore, an irradiated area of 10 cm × 10 cm appears to be a reasonable approximation for the dimensions of the target. The whole area of the target is set to 12 cm × 12 cm. Long lifetime and thermal load capacity, particularly with 6 MW pulse height, are achieved through a suitable choice of material and a suitable engineering design. Reliability and compactness are further enhanced by the focus on a stationary target design instead of a rotating target or liquid target.

2.1. Material selection

From materials studies in the field of target development for spallation sources [22,23] we identify within the material range of $70 < Z < 82$ [21], tantalum and tungsten as the most promising materials to design a high performance target for HBS.

Tantalum was chosen because, along with tungsten, it has one of the best neutron yields [24] of about 0.14 neutron per incident proton at the selected energy of 70 MeV. This leads to the total neutron yield of $\sim 1.0 \times 10^{15}\,\mathrm{s}^{-1}$ [20] for protons with a power of 100 kW as calculated with MCNP version 6.1 [25] using ENDF/B-VII database [26].

Tantalum is superior to tungsten in terms of machinability and weldability and in terms of hydrogen solubility i.e. it has a high blistering threshold. Hydrogen embrittlement is one of the main risks concerning target integrity at CANS (e.g. [27]) and must be taken into account especially at HiCANS due to the high proton beam current. Hydrogen embrittlement is caused by proton accumulation and the creation of hydrogen bubbles [28] since the protons lose energy as they penetrate the target material and are stopped inside the target. In order to minimize the risk of hydrogen embrittlement, the following measures are taken: (i) The target is made of tantalum which can absorb a high amount of hydrogen (0.76 H/Ta atom) and retains its properties up to a hydrogen content of approx. (0.175 H/Ta atom [29]) (ii) The amount of protons stopped inside the target is minimized by adjusting the target thickness in such a way that the average proton exit energy is close to the threshold of the neutron releasing (p,xn) reactions at tantalum at 7.6 MeV according to the TENDL-2021 database [30]. According to SRIM (The Stopping and Range of Ions in Matter) [31] the penetration depth is 5.09 mm for 70 MeV protons inside tantalum. Subtracting the penetration depth of about 0.14 mm for 7.6 MeV protons, the target thickness results in 4.95 mm as a compromise between best neutron output and minimum hydrogen implantation. Two studies with FLUKA [32] showed that at this chosen tantalum thickness, the target lifetime in terms of proton and neutron-induced displacements per atom (dpa) is significantly longer than a year [33,34].

In addition, tantalum exhibits, besides a high melting point, a suitable combination of thermo-mechanical properties such as high thermal conductivity, low thermal expansion coefficient to reduce thermal and particularly fatigue stress, good elasticity and ductility and high yield strength to act as a solid target [35]. These properties are

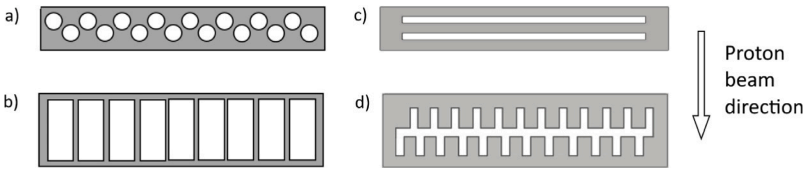

Fig. 1. Preliminary considerations resulting in the actual cooling channel arrangement: (a) row of holes, (b) channels aligned parallel to the proton beam, (c) channels aligned perpendicular to the proton beam, (d) combination of (b) and (c).

very important since the target has to withstand a range of temperature differences and stress. Furthermore, it has a low chemical reactivity and low radiation damageability which are essential for physico-chemical stability.

2.2. Cooling considerations

Considering a target area of $100\,\mathrm{cm}^2$ and a time-average thermal load of $100\,\mathrm{kW}$ a heat load of $1\,\mathrm{kW\,cm}^{-2}$ must be dissipated. Studies from the chip industry [36] and neutron target development show that microchannel heat sinks are suitable for dissipating heat flows of this order of magnitude. For example it was demonstrated in [37] that an efficient single-phase cooled microchannel is able to remove up to $3.5\,\mathrm{kW\,cm}^{-2}$ from a cylindrical beryllium neutron target ($\mathrm{d} = 1.2\,\mathrm{cm}$) using copper micro tubes of $0.5\,\mathrm{mm}$ diameter attached to the targets bottom.

Thus, a cooling structure integrated into the target was developed. This internal heat dissipation has three decisive advantages compared to a heat sink connected on one side: (i.) The amount of material is reduced. (ii.) There is no interface between the target and a heat sink and hence no critical region for hydrogen accumulation nor a strong shear force generation driven by different thermal expansion coefficients. (iii) The temperature profile inside the target is homogenized.

Fig. 1 shows different considerations that led to the final design of the microchannel cooling structure. The simplest micro cooling arrangement inside a target consists of a row of small holes through the target perpendicular to the proton beam as shown in Fig. 1 (a). However, the free flow cross section of simple holes is too small to remove the entire heat load and the manufacturing of such small holes is expensive, time-consuming and error-prone. Thin channels aligned parallel to the proton beam as (Fig. 1b), increase the flow cross-section but create in-homogeneous proton penetration depth due to alternating coolant and bridge sections. Thin cooling channels aligned perpendicular to the proton beam as (Fig. 1(c), solve the issue of in-homogeneous proton penetration depth but lack in terms of sufficient free flow cross section and offers only minor interface area for heat transfer to the coolant. Finally, the channel arrangement is a microchannel structure combined of the channels aligned perpendicular and parallel to the proton beam direction as shown in Fig. 1(d). This so called "lamella structure" improves the heat dissipation efficiency, as a large proportion of the total tantalum volume, namely each part between two vertical channels act as a cooling fin. Additionally, this combination provides sufficient coolant flow and interface area. Based on this lamella structure, a cooling design is realized that ensures an equal penetration depth for each incoming proton by placing two of the lamella structures one behind the other as sketched on left hand side in Fig. 3.

2.3. Microchannel parameter

Channel thickness

The width of the microchannels is limited by the manufacturing technology. Production tests, which preceded the production of the first target in 2019, have shown that uniform and reproducible channels with a diameter of down to 0.35 mm can be eroded through $12\,\mathrm{cm}$ tantalum thickness using electrical discharge machining (EDM). Channels with $0.35\,\mathrm{mm}$ width offer a good compromise between acceptable water pressure drop, good heat transfer coefficients and sufficient coolant flow. With narrower channels, the erosion-wire frequently breaks and creates offsets. The erosion of wider channels is possible but the heat transfer and the interface area both drop quickly with increasing channel thickness as well as the number of possible arrangements.

Coolant Velocity

The pressure loss as well as the heat transfer coefficient depend on the flow velocity and its three possible types of flow regimes laminar, transitional and turbulent. Fig. 2 shows the correlation between these three regimes for $0.35\,\mathrm{mm}$ wide microchannels. The pressure loss increases quadratically with the flow velocity in the laminar range, the heat transfer coefficient increases with an exponent of 1/3 with increasing flow velocity. In the transition range between $2.25\,\mathrm{m\,s}^{-1}$ and $5.25\,\mathrm{m\,s}^{-1}$, the heat transfer coefficient increases steeply. From the turbulent flow range onwards, the heat transfer coefficient increases linearly. The target coolant velocity should hence be well within the turbulent regime to benefit from the strong heat transfer coefficient in this region. At the same time, it must be ensured that a high pressure drop does not lead to unacceptably high stresses in the target. The minimum pressure loss inside the turbulent region is $1.25\,\mathrm{bar}$. A mechanical analysis of the target is therefore necessary to estimate the stresses caused by the coolant pressure.

Stress consideration

Mechanical stress can endanger the targets mechanical stability and is one of the main limiting factors in terms of achievable power density. Stresses are generated by thermal strains, internal forces and external forces. The thermal stresses are investigated within Section 4.2 "Finite Element Method". The external forces are only caused by the coolant pipes because these two are the only fastening and the target will be operated in a vacuum. The coolant pipes are regarded as fixed bearings and the strain generated by this connection have been minimized in the design process and can be neglected. Internal forces are generated by the pressure gradient between the coolant and the vacuum surrounding the target. In order to estimate the stress generated by the coolant pressure, the internal cooling structure consisting of two rows of microchannels as discussed in Section 2.2 and shown on the left hand side in Fig. 3 must first be finalized.

The most loaded regions are the $0.8\,\mathrm{mm}$ thin tantalum layers between the coolant and the vacuum as shown in Fig. 3 (a). These thin layers can neither be increased nor reinforced with ribs, as this would change the target thickness and thus would cause issues with hydrogen implantation. However, the stresses can be limited by reducing the unsupported width of the thin layers by dividing the two rows of microchannels into narrow segments as sketched in Fig. 3 (b).

The basic relationship between the stress, the width w (m) of a single segment, the water pressure p (Pa) and the thickness of the thin tantalum layer h (m) can be illustrated by considering each segment as a so called equally loaded rectangular plane plate with fixed edges. The dominant bending stress σ (Pa) of such a system can be estimated as [39]:

$$\sigma = x \cdot \frac{p \cdot w^2}{h^2}, \tag{1}$$

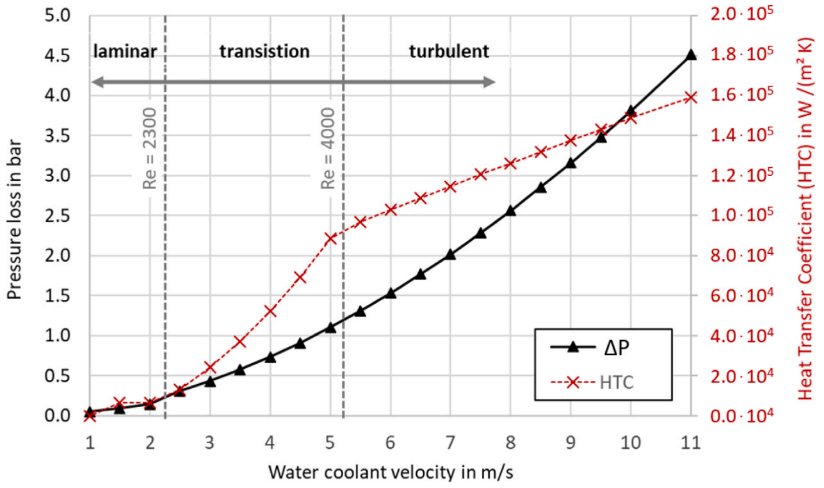

Fig. 2. Effects of coolant velocity on pressure loss (ΔP) and heat transfer coefficient (HTC) inside 0.35 mm wide microchannels for a 12 cm target length. Values are estimated based on correlations according to [38], Re is the Reynolds number.

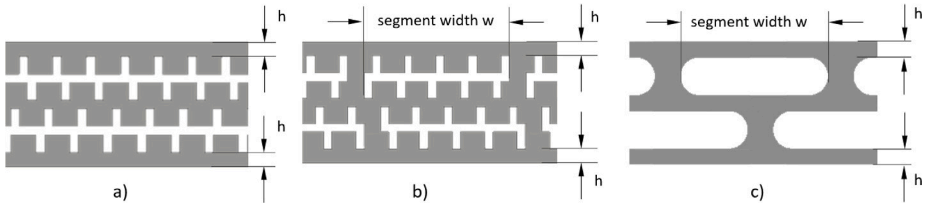

Fig. 3. Basic micro channel structure consisting of two lamella structures one behind the other as discussed in Section 2.2(a), design with reduced segment width (b) and simplified design with maximized radii for preliminary FEM parameter study (c).

where the factor x depends on the ratio of segment width w to length in flow direction and was selected in [39]. The highest stresses occur at the ends of the individual segments. These stresses are reduced by adding radii at the edges as shown in Fig. 3(c). An analytical calculation of the stresses is no longer practicable, so therefore a parameter study was carried out using FEM.

Fig. 4 shows the correlation between the total coolant pressure p and the pressure induced stress σ for various segment width calculated with FEM using the simplified cooling geometry as shown in Fig. 3(c). The static coolant pressure is set to 3 bar downstream of the target. This pressure appears to be sufficient to compensate for pressure losses in the return line as well as to keep the pressure sufficiently high to suppress boiling processes downstream. A safety factor of 1.3 according to [40] is set to the yield strength (172 MPa) [35] of tantalum which leads to 132 MPa. This upper limit of the permissible stress represented by the horizontal dark blue dashed line.

Around 105 mm of the target width should include microchannel segments in order to reliably cover the entire illuminated surface resulting in possible segment widths of 21 mm, 17.5 mm, 15 mm or 13 mm. 15 mm wide segments were chosen as these are the longest segments where the pressure loss is larger than 2.5 bar and thus realizing a flow in the turbulent regime.

Effective proton penetration depths

The influence of the internal cooling structure on the proton energy loss was investigated using MCNP6.1. Ideally, all protons leave the target with an energy just below the threshold value for the release of free neutrons. Since the coolant structure affects the proton energy loss, the energy spectrum of the outgoing proton beam behind the target was used to determine this influence. A 5 mm thick, pure tantalum target serves as the reference case which is illuminated with a 70 MeV proton beam. The pure tantalum target is compared to the target with internal cooling structure in lamella design as shown in Fig. 5 (b). The total thickness of the lamella design target is adjusted to 6.5 mm to compensate for the lower stopping power of protons inside the cooling structure. The energy spectra of the outgoing protons are shown on the left-hand side of Fig. 5. In the "pure tantalum" case the average energy is 6 MeV and the energy spectrum extends to 18 MeV. For the "lamella design" the average energy spectrum rises to 16.7 MeV and extends to a maximum of 42 MeV. Note that the spectrum has a second maximum at 28 MeV and a plateau between 15 MeV and 25 MeV. Since the projected tantalum thickness and thus the proton stopping range in solid tantalum and in the lamella design should theoretically be the same, these effects are most likely caused by an unfavourable microchannel geometry. The free path of protons inside water is significantly higher compared to tantalum and thus the energy transfer per path length is about 6 times smaller resulting in streaming paths for protons. This density driven leakage effect is comparable to narrow gaps in radiation shielding. Examples of possible leakage paths are outlined in Fig. 5 (b). Since each possible path cause a different energy loss, the proton energy spectrum shows all possible paths integrated over the probability as a histogram.

A slight inclination of the channels minimizes this proton leakage. This new "fishbone design" as shown at Fig. 5(c) has a thickness of 6.34 mm. The inclined channels reduce the chance of protons passing through the target without interaction, thus homogenizing the energy loss of the protons. The average outgoing proton energy is now reduced to 10.8 MeV and the energy spectrum extends to 30 MeV. With this design, neutron production is maximized while at the same time the Bragg peak is behind the target, minimizing hydrogen implantation.

3. Target design

The basic design of the entire target is shown Fig. 6. It consists of the neutron producing main body and two adjacent coolant supply tubes welded on. The entire assembly is made of pure tantalum. The main body weighs 1.1 kg and the weight of each coolant supply is 0.7 kg. The water coolant enters the microchannel structure inside the targets

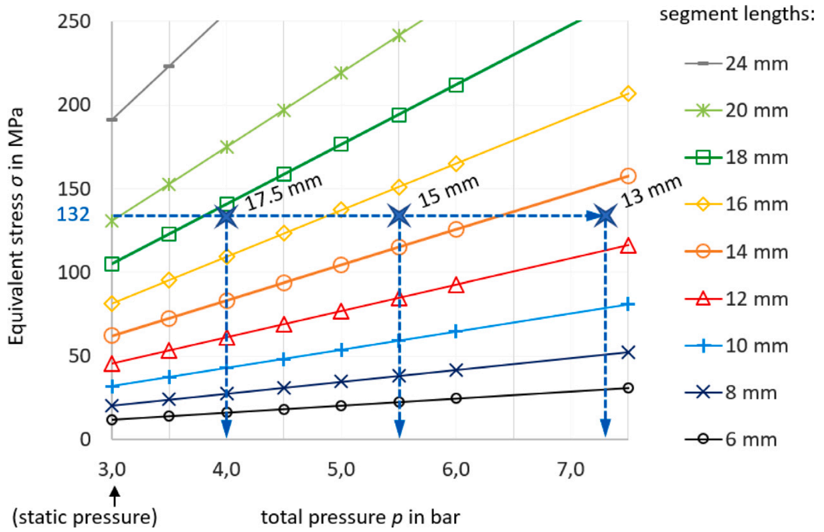

Fig. 4. Correlation between total coolant pressure p inside the target, microchannel segment width w and resulting equivalent stress σ. The dashed line at 132 MPa indicates the set upper stress limit. The three vertical dashed lines show permissible coolant pressures for possible microchannel segment width.

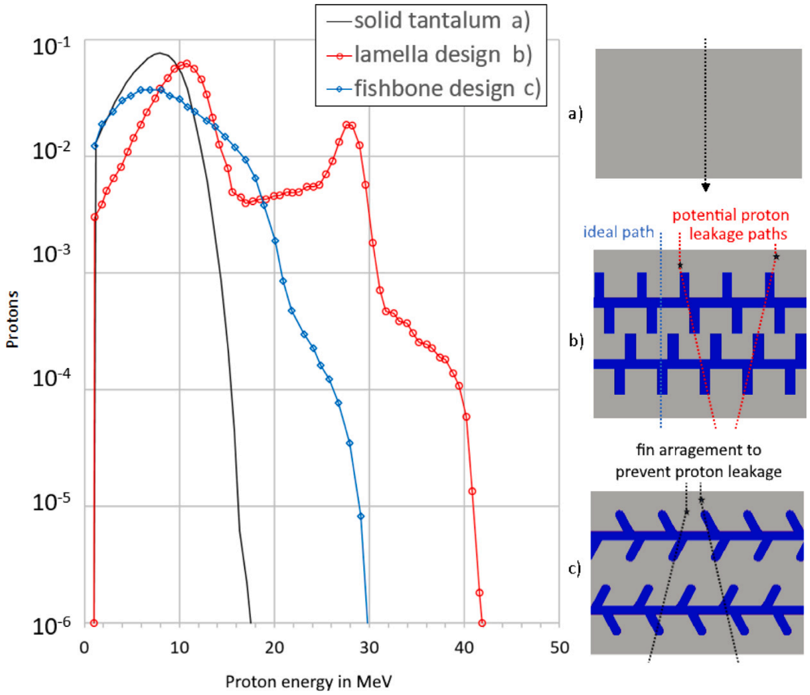

Fig. 5. Effects of coolant channel design on the proton spectrum behind tantalum targets irradiated by a 70 MeV proton beam, (a) pure tantalum (5 mm thick) (b) lamella design (6.5 mm thick) (c) fishbone design (6.34 mm thick).

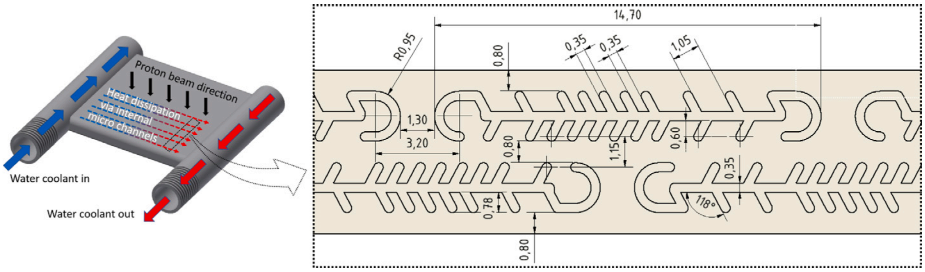

Fig. 6. Target with coolant supply tubes (left) and cross section through the main body: neutron producing tantalum layer with inner microchannel structure (right).

Table 2
Parameter of the CFD simulation.

meshing parameters	
number of nodes	8.1×10^6
sweep division in flow direction	40
first layer height (interface inflation)	1×10^{-6} m
y+ (max./average)	1.84/0.78
boundary parameter	
inlet mass flow	1.34 kg s^{-1}
inlet temperature	20 °C
outlet pressure	3 bar
heat release inside entire target	89.14 kW
heat load inside microchannels	4.18 kW
simulation results	
pressure loss inside microchannels	2.0 bar
inlet pressure	5.0 bar
average coolant velocity	8 m s^{-1}
highest tantalum temperature	161.6 °C
highest interface temperature	119.9 °C
water heat up	15.6 °C
highest interface heat flux	4.4×10^6 W m^{-2}

main body through a supply tube with a coolant mass flow of 1.37 kg s^{-1} and around 5 bar. The water coolant is pressed into the microchannels through a groove in the side of the supply tube, absorbs the heat from the tantalum as it flows through and is further guided into an outlet tube.

The neutron producing layer shown in Fig. 6 has two alternating rows of 14.7 mm wide microchannels segments and a free flow cross section of 171 mm^2 in total. Vertical branches of the channels have been inclined by 28° regarding the vertical direction to prevent proton leakage. The two ends of the channel segments are designed as rounds with a radius of 0.95 mm, the maximum possible radius, to minimize the stresses in this region. The density of the inclined branches varies depending on the opposing microchannel geometry to ensure a constant stopping power for each proton.

4. Simulations

The engineering phase focuses primarily on improving heat dissipation and reducing mechanical stresses by adapting the cooling structure. The CAD program Autodesk Inventor is used to create the geometry. This geometry is transferred to the CFD (Computational Fluid Dynamic) simulation software ANSYS CFX 2019 R3 which is used to analyse the flow and calculate the heat flows and temperature distribution. The temperature field, coolant pressure distribution and the geometry are then loaded into the FEM (Finite Element Method) software ANSYS Mechanical 2019. The FEM analyses are performed to calculate the local stresses and to evaluate the selected coolant velocity. The results from the CFD and FEM simulations are then used to iteratively revise the geometry, e.g. to reduce stress peaks and homogenize the temperature field. Fig. 6 shows the geometry at the final stage of the optimization process. It shows a repeating microchannel segment from the cross section through the target.

4.1. Computational fluid dynamics

Within the CFD simulation the entire main body of the target is simulated three-dimensionally, including the entire cooling structure, without any geometric simplifications. However, the supply tubes are modelled by boundary condition which does not influence the flow inside the microchannel due to the high pressure drop inside the microchannel (about 2 bar) compared to the minor pressure drop inside the DN 20 supply tubes across the target width (about 200 Pa).

Table 2 summarizes the most important meshing and boundary parameters. Each microchannel segment is meshed on the face with inflation layers starting at the interface to the solid and stretched across the volume using the sweep method. Each microchannel segment front face is defined as an inlet, and each back face is defined as an opening. The simulation is treated as a static problem. Tantalum is defined as a solid material with a temperature depended thermal conductivity. The microchannel segments are defined as a fluid domain using the formulation of the thermodynamic properties of water IAPWS-IF97 [41]. The energy release of the proton beam is modelled by a volumetric source. Orthogonal to the proton beam direction, the heat source is confined by a step function (on/off) to an area of 10 cm × 10 cm. The volumetric heat release within the target thickness is calculated with the program SRIM for a homogeneous mixture consisting of 78.5 vol.% tantalum and 21.5 vol.% water. In the simulation, the volumetric energy release is reduced to one sixth in the water domain and the total energy release in the target is subsequently normalized to 91.5% of the initial energy carried by the proton beam. The actual heat release is displayed in top left side of Fig. 7. The outgoing proton beam is assumed to have a remaining energy of 7.6 MeV and hence 10.86 kW residual energy which is deposited outside the target.

In the lower section of Table 2 the most relevant results of the CFD simulations are summarized. The resulting pressure loss of 2.0 bar in the microchannel structure is below the estimated value of 2.5 bar according to Fig. 2. This is probably due to the complex channel geometry where locally the ratio of fluid volume to surface area is increased by the branches of the fishbone design. Fig. 7 (bottom) shows the resulting temperature distribution within the cross section through the target perpendicular to the flow direction at the position with the maximum temperature. The temperature is highest at the bottom of the target where the protons have the highest energy release. The lowest temperatures are located between both microchannel rows. Between the branches of the cooling channels, the cooling is optimal due to the large surface-to-volume ratio. Temperature maxima are located at the tantalum bridges between microchannel segments within a row due to the low ratio of tantalum volume to interface[1] surface. However, the maximum interface temperature of 119.9 °C is below the boiling temperature of the cooling water (133.2 °C at 3 bar). The interface heat flux seems very high and will be considered next in subsequent investigations in order determine the effects of possible nucleate boiling.

4.2. Finite element method

The FEM simulations are based on the temperature distribution and the dynamic coolant pressure provided by previous CFD simulations. As part of the CFD simulation, the cooling water velocity was varied to determine the optimal value. The results are shown in Fig. 8. As the flow velocity increases, the heat transfer at the interface between the target and the cooling water increases linearly and the average cooling water temperature decreases. This causes the temperatures in the target to drop. At the same time, the increase of the flow velocity causes a quadratic increase of the pressure drop and thus an increase of the pressure induced stresses. Based on these CFD results, the subsequent mechanical simulations calculate the behaviour of the equivalent stress for different coolant flow rates, as shown in Fig. 8.

The graph indicates that the lowest stress values can be expected at flow velocities around 10 m/s. Lower velocities reduce the pressure-induced stress but increase temperature-induced stress. For higher velocities the pressure loss becomes dominant in relation to the temperature-induced stress and hence the total stress rises. However, the mechanical stresses are below the failure limits of tantalum for

---

[1] According to the Pre-CFX Users Guide “domain interfaces are required to connect multiple unmatched meshes within a domain (...) and to connect separate domains”. In this case, the interface connects the solid tantalum domain with the liquid coolant domain and manages the heat transfer.

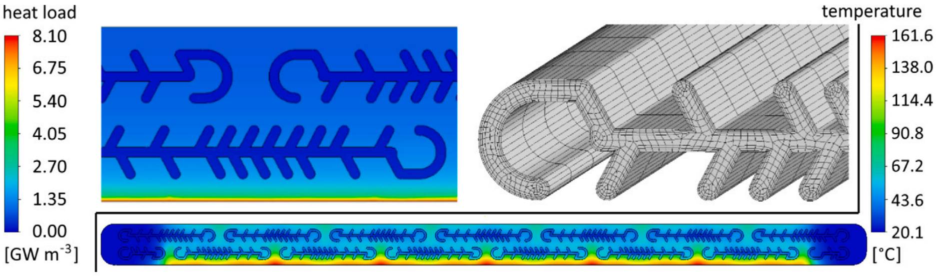

Fig. 7. CFD simulation of the HBS target: top left: heat source at 100 kW, top right: detailed view of CFD mesh of the micro channels, bottom: Cross Section through the target perpendicular to the flow direction at the position with the maximum temperature.

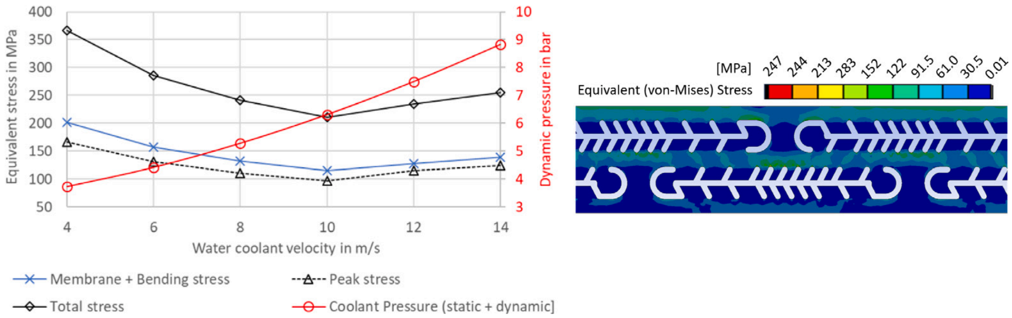

Fig. 8. Effects of coolant velocity on equivalent stress, based on ANSYS FEM simulation (right) and representative equivalent stress contour plot with 8 m/s coolant velocity (left).

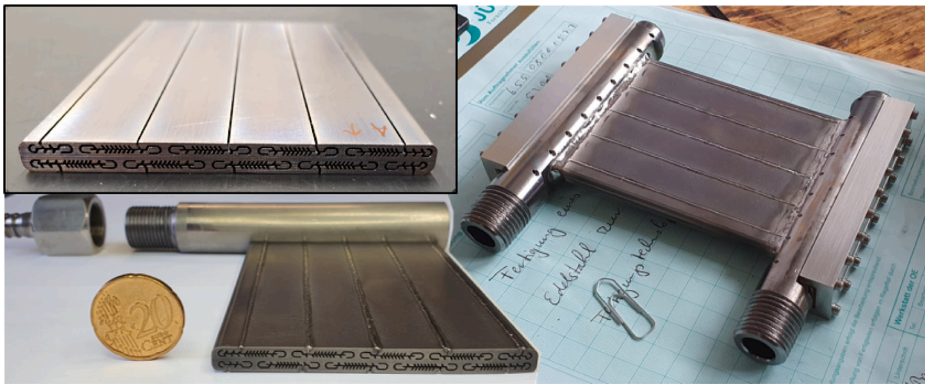

Fig. 9. Target with microchannel structure right after the wire erosion process at PGI-JCNS workshop in Forschungszentrum Jülich. The entry channels of the erosion wire can be seen on the surface (top left). Target with welded entry channels (bottom left), test target with welded supply lines (right).

flow velocities above 6 m/s. On the downside higher velocities increase mechanical loads such as the erosion rate and increase the risk of cavitation at the exit of the microchannels. Erosion resistance cavitation was investigated at 8 m/s as part of an inhouse experiment shown in Section 5.3. Based on these investigations and in view of the mechanical stresses, a speed of 8 m/s was selected.

5. Experimental validation

5.1. Prototype tantalum target

A prototype target was manufactured to perform load and erosion tests and to confirm the manufacturing method. The main body width is reduced from 116 mm to 76.4 mm and hence the number of parallel microchannel segments is reduced by 5 segments. The length of the main body is reduced from 120 mm to 100 mm. The thickness of the main body is 6.2 mm. Both supply tubes of the test target have an additional groove as a window for inspection of the microchannels.

5.2. Manufacturing

The microchannels are created via wire EDM (Electrical Discharge Machining). Each segment is eroded separately by a 0.25 mm wire coated with zinc which enters the target from the surface. Each entry creates a 0.35 mm wide groove at the targets surface which is shown in the upper right side in Fig. 9. The tantalum target is degreased, cleaned in an ultrasonic bath and finally pickled in acid. The aim of cleaning is to completely remove residues from the erosion process (especially copper) before subsequent welding.

The subsequent welding processes are done without additives under argon atmosphere (gas purity 5.0) inside a welding dome. An overpressure of 3 mbar to 4 mbar prevents the ingress of oxygen. A oxygen measuring device is used to ensure that the residual oxygen in the welding process is consistently below 10 ppm. This low concentration is necessary due to the high affinity of Ta to H_2 and O_2 above 300 °C.

The grooves at the surface are closed via laser welding. For this purpose, strips of tantalum sheet are stuck into the grooves, melted by the laser, and thus fuse with the target. The strips are melted alternately on the top and bottom of the target to prevent it from

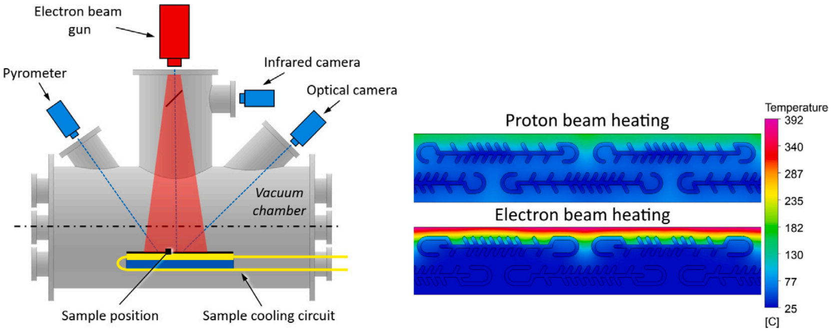

Fig. 10. JUDITH-2 basic design, drawing is based on [42] (left), and exemplary comparison of the temperature distributions at the target cross section caused by proton beam and electron beam heating, both at average beam power of 1 kW/cm^2 simulated with ANSYS CFX (right).

Table 3
Tantalum concentration inside cooling water during 6 week erosion test.

elapsed test time [days]	Ta concentration [μg/L]
0 (2.3 h)	8.0 ± 1.5
12	3.8 ± 0.6
28	1.8 ± 0.6
35	≤2.0
46	≤2.0

bending. After hardening, external bulges appear, which are ground off. The connecting tubes are welded to the target using TIG (Tungsten Inert Gas) welding with Helium–Argon welding gas. The weld joints are designed as lap joints for a fillet weld. The filler metal is a 0.8 mm thick tantalum wire.

A measurement of the microchannels via light microscope shows that the basic structure of the microchannels is very precisely eroded, but the individual fins are on average approx. 20% too thick, 0.43 mm instead of 0.35 mm. A detailed measurement of the manufacturing tolerances and the deviations can be found in [34].

5.3. Erosion test

The resistance of the microchannels to erosion caused by the cooling water was demonstrated in a six-week endurance erosion test. The target was streamed with 1.3 kg/s fully deionized water (equivalent to 8.9 m/s inside the microchannels) at 40 °C. Five water samples were taken during the endurance test and analysed with ICP-MS (inductively coupled plasma mass spectrometry) at ZEA-3 at Forschungszentrum Jülich. The highest tantalum concentration was measured right after the start of the endurance test as shown in Table 3. This indicates that there were tantalum residue in the microchannels that originated from fabrication. These residue were released by the water at the beginning of the erosion test. A total of about 0.38 μg of tantalum inside the coolant circuit was estimated. During the experiment, the tantalum concentration decreased by a factor of 4 within 4 weeks and then remains below the detection limit. The decrease in initial concentration indicates that the initial tantalum residue settle over time and only marginal amounts of tantalum particles are constantly eroded which are not relevant for the technical operation of the target. However, the measurements of the tantalum residue clearly show that the cleaning procedure for the microchannels during production needs to be improved.

Optical measurements to compare the channel thickness before and after the erosion test as well as a constant monitoring of the pressure loss do not show any changes in the dimension and the geometry of the channels. However, varying the pressure in the outlet of the microchannels produced reproducible audible cavitation below a static pressure of 1.7 bar. This threshold value increases with increasing temperature and speed. However, a static pressure of 3 bar in flow direction behind the target during operation should provide sufficient safety.

5.4. Heat load test

The target was successfully tested with a high heat flux of up to $1\,\mathrm{kW\,cm^{-2}}$ in the electron beam facility JUDITH-2 [42] at Forschungszentrum Jülich. The basic design of the JUDITH-2 facility is shown on the left side of Fig. 10. The target placed inside the vacuum chamber is heated on the upper side on an area of 60 mm × 80 mm with an electron beam and is connected to the water cooling circuit system via the targets supply tubes. The electron gun scans a focused beam over the target surface. The edges of the heated zone are shaded by copper cooling elements. The water coolant enters the target with 20 °C and approx. 7 bar with an average velocity inside the microchannels of $8.2\,\mathrm{m\,s^{-1}}$. The target surface temperature is measured at 20 Hz with an infrared camera which was calibrated for tantalum. The energy absorbed by the target is determined by the temperature difference of the cooling water as it flows through the target.

In the course of the experiment the absorbed power of the electron beam is gradually increased up to $1\,\mathrm{kW\,cm^{-2}}$ in increments of about $0.05\,\mathrm{kW\,cm^{-2}}$. After each power change, the surface temperature reaches a steady state after less than 2 s and it was kept constant for at least 30 s.

The major difference between heat input using an electron beam and heat input using a proton beam is the penetration depth. The electron beam power is deposited in the first few micrometres of the target since JUDITH-2 run with a low acceleration voltage of about 40 kV to benefit surface heating and reduce volumetric heating. As a result, only the part of the cooling structure facing the surface contributes to heat dissipation as sketched on the bottom right-side of Fig. 10. In contrast, a proton beam cause volumetric heating over the entire targets depth and hence the whole cooling structure contributes to the cooling and leads to lower temperatures. As a result, the surface temperatures in the JUDITH-2 experiment are above the expected temperatures caused by a proton beam with the same thermal power density. However, the CFD simulation of the JUDITH-2 experiment is used to validate the CFD model of the target in order to be able to make reliable calculations of the temperature behaviour in the case of the proton beam with this validated model.

A qualitative comparison between measured and simulated temperatures at different powers is shown in Fig. 11. The cooling water flows from the left to the right in each image. It is noticeable that the surface temperatures are not homogeneous. In both, the measurement and the simulation, a temperature profile orthogonal to the flow direction can be seen in addition to a temperature increase in the flow direction. This orthogonal temperature profile is created by the geometry of the cooling channels, illustrated by the image of the cross-section of the

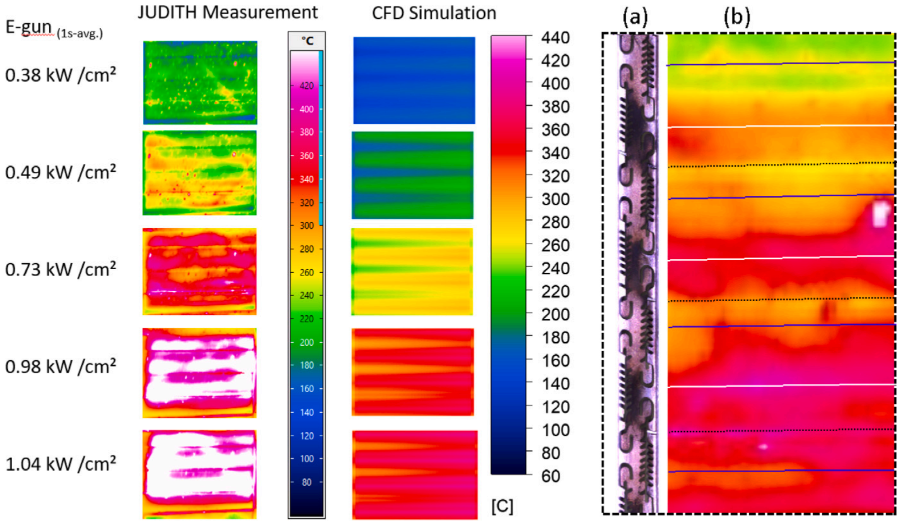

Fig. 11. Comparison of the surface temperatures from IR measurement and CFD simulation (left side) and (a) cross section of the microchannels perpendicular to the (b) enlarged section of a single IR image at a power of 0.72 kW/cm^2 (right side).

target at the right side of Fig. 11. The tantalum bridges between the individual cooling channel segments create the areas with the highest temperatures on the surface (white lines). The cooling channel areas with the regular microchannel structure have the most effective cooling and hence the lowest surface temperature (blue lines). The welded areas on the surface (dashed black lines) have different temperatures. The thermal connection of the welds therefore appears to vary strongly. The temperature increase in flow direction is caused by the temperature increase of the cooling water. All these influences except the welds are included in the CFD simulation. The resulting surface temperature profiles match well in simulation and measurement. While the local temperature distribution as well as the general trend over the power agrees well between experiment and simulation, it is already noticeable that the simulation consistently underestimates the temperatures. However, the experiment proved the ability of the target to operate at $1\,\mathrm{kW\,cm^{-2}}$ even under the very conservative one-sided heat load.

6. Conclusion and outlook

The HiCANS facility HBS requires the development of a new type of target due to its unique characteristics consisting of a proton beam with $70\,\mathrm{MeV}$, $1.67\,\mathrm{mA}$ average beam current and a $100\,\mathrm{kW}$ thermal load. A stationary solid target made of tantalum was developed with a novel internal microchannel cooling structure. The target is suited for windowless operation in vacuum. It pays attention to known problems of CANS targets such as hydrogen embrittlement by using tantalum as the target material, which has excellent storage properties for hydrogen and by placing the proton Bragg peak outside the target. The microchannel geometry of the target was iteratively optimized using CFD and FEM methods under operating conditions to homogenize the temperatures and to minimize the mechanical stresses. An initial prototype of the target was successfully manufactured as part of a production testing project. The heat dissipation capacity of the cooling structure was successfully demonstrated with an electron gun at a surface heat flux of $1\,\mathrm{kW\,cm^{-2}}$. The resistance of the microchannel structure to abrasion caused by erosion was demonstrated as part of an endurance test.

Nevertheless, potential for improvement was identified. The manufacturing technology must be further developed to ensure production maturity with reliable tolerances and to establish a manufacturing process which avoids the weld lines at the target surface. A cleaning process must be developed to reliably remove the tantalum residue from production. Optimization of the target with regard to neutron release and homogenization of the heat deposition caused by the proton beam is planned. In addition, the target can be extended by an integrated water beam stop. This beamstop could consist of a tantalum shell behind the target that is circulated with cooling water. This additional water layer would not only stop the proton beam and hence protect the environment of the target from hydrogen implantation but also improve the heat dissipation at the back of the target, the region with the highest heat release.

CRediT authorship contribution statement

J. Baggemann: Writing – original draft, Methodology, Investigation, Conceptualization. **T. Gutberlet:** Writing – review & editing, Supervision, Resources, Project administration. **P. Zakalek:** Writing – review & editing, Software, Methodology, Formal analysis. **J. Wolters:** Writing – review & editing, Validation, Software. **U. Rücker:** Methodology, Investigation. **E. Mauerhofer:** Writing – review & editing, Investigation, Conceptualization. **J. Li:** Software, Investigation. **Q. Ding:** Software, Investigation. **Th. Loewenhoff:** Validation, Resources, Investigation. **D. Dorow-Gerspach:** Resources, Investigation. **Y. Bessler:** Software, Conceptualization. **Th. Brückel:** Resources, Methodology, Investigation.

Declaration of competing interest

The authors declare that they have no known competing financial interests or personal relationships that could have appeared to influence the work reported in this paper.

Data availability

Data will be made available on request.

Acknowledgement

We thank the PGI-JCNS workshop team in Forschungszentrum Jülich for the successful fabrication of the HBS target and are particularly thankful for the intensive exchange of ideas during the production test phase, which is what made production possible in the first place.

References

[1] B. Riemer, M. Wohlmuther, H. Takada, N. Takashi, Spallation target developments, in: Thorium Energy for the World, Springer International Publishing, 2013, pp. 273–277.

[2] F. Foroughi, R. Bercher, C. Büchli, R. Meyer, PSI - Scientific and Technical Report 1999, Tech. Rep, Paul Scherrer Institut, (ISSN: 1423-7350) 2000.

[3] L.G. Jones, D. Wilcox, ISIS TS1 project target – design for manufacture, Phys.: Conf. Ser. 1021 (2018) 012056.

[4] S. Wei, R. Zhang, Q. Ji, C. Li, B. Zhou, Y. Lu, J. Xu, K. Zhou, C. Zhao, N. He, W. Yin, T. Liang, Overview of CSNS tantalum cladded tungsten solid Target-1 and Target-2, Nucl. Eng. Technol. 54 (2022) 1535–1540.

[5] S. Wei, Q. Ji, X. Jia, R. Zhang, K. Zhou, T. Liang, Advance of CSNS solid target, in: Materials Science Forum, Vol. 1024, 2021, pp. 151–155.

[6] L. Zavorka, M.J. Mocko, P.E. Koehler, Physics design of the next-generation spallation neutron target-moderator-reflector-shield assembly at LANSCE, Nucl. Instrum. Methods Phys. Res. A 901 (2018) 189–197.

[7] A. Nelson, J. O'Toole, R. Valicenti, S. Maloy, Fabrication of a tantalum-clad tungsten target for LANSCE, J. Nucl. Mater. 431 (1) (2012) 172–184, Special Issue of the Tenth International Workshop on Spallation Materials Technology, (IWSMT-10).

[8] A. Aguilar, et al., Design specification for the european spallation source neutron generating target element, Nucl. Instrum. Methods Phys. Res. A 856 (2017) 99–108.

[9] J.R. Haines, T.J. McManamy, T.A. Gabriel, R.E. Battle, K.K. Chipley, J.A. Crabtree, L.L. Jacobs, D.C. Lousteau, M.J. Rennich, B.W. Riemer, Spallation neutron source target station design, evelopment, and commissioning, Nucl. Instrum. Methods Phys. Res. A 764 (2014) 94–115.

[10] B. Riemer, J. Janney, S. Kaminskas, D. Mcclintock, P. Rosenblad, Target operational experience at the spallation neutron source, in: 11th International Topical Meeting on Nuclear Applications of Accelerators, AccApp 2013, 2013, pp. 359–365.

[11] S. Sakamoto, et al., Technical Design Report of Spallation Neutron Source Facility in J-PARC, JAEA, 2012.

[12] T. Rinckel, D. Baxter, J. Doskow, P. Sokol, T. Todd, Target performance at the low energy neutron source, Physics Procedia 26 (2012) 168–177, proceedings of the first two meetings of the Union of Compact Accelerator-Driven Neutron Sources.

[13] Y. Yamagata, K. Hirota, J. Ju, et al., Development of a neutron generating target for compact neutron sources using low energy proton beams., J. Radioanal. Nucl. Chem. 305 (2015) 787–794.

[14] T. Kobayashi, S. Ikeda, Y. Otake, Y. Ikeda, N. Hayashizaki, Completion of a new accelerator-driven compact neutron source prototype RANS-II for on-site use, Nucl. Instrum. Methods Phys. Res. A 994 (2021) 165091.

[15] I. Mardor, O. Aviv, M. Avrigeanu, D. Berkovits, A. Dahan, T. Dickel, I. Eliyahu, M. Gai, I. Gavish-Segev, S. Halfon, M. Hass, T. Hirsh, B. Kaiser, D. Kijel, A. Kreisel, Y. Mishnayot, I. Mukul, B. Ohayon, M. Paul, A. Perry, H. Rahangdale, J. Rodnizki, G. Ron, R. Sasson-Zukran, A. Shor, I. Silverman, M. Tessler, S. Vaintraub, L. Weissman, The Soreq Applied Research Accelerator Facility (SARAF): Overview, research programs and future plans, Eur. Phys. J. A 54 (91) (2018).

[16] A. Kreisel, I. Eliyahu, S. Vintraub, et al., Neutron and isotope production yield from proton and deuteron beams in the 20–45 MeV range on thick liquid gallium-indium and lithium targets, Eur. Phys. J. A 59 (185) (2023).

[17] I. Eliyahu, G. Berkovic, S. Vaintraub, et al., Optical Measurements of the thickness of the Gallium Indium free surface jet for the SARAF beam dump and neutron source, Nucl. Instrum. Methods Phys. Res. A 1053 (2023) 168320.

[18] J. Schwindling, B. Annighöfer, N. Chauvin, J.-L. Meuriot, B. Mom, F. Ott, N. Sellami, L. Thulliez, Long term operation of a 30 kW Beryllium target at IPHI, J. Neutron Res. 24 (2022) 289–298.

[19] M. Pérez, F. Sordo, I. Bustinduy, J.L. Muñoz, F.J. Villacorta, ARGITU compact accelerator neutron source: A unique infrastructure fostering R & D ecosystem in Euskadi, Neutron News 31 (2–4) (2020) 19–25.

[20] T. Gutberlet, et al., Technical Design Report HBS, Volume 2 – Target Stations and Moderators, Tech. Rep., JCNS, Forschungszentrums Jülich, 2023.

[21] P. Zakalek, P.-E. Doege, J. Baggemann, E. Mauerhofer, T. Brückel, Energy and target material dependence of the neutron yield induced by proton and deuteron bombardment, EPJ Web Conf. 231 (2020) 03006.

[22] G. Bauer, Overview on spallation target design concepts and related materials issues, J. Nucl. Mater. 398 (1) (2010) 19–27, proceedings of the Ninth International Workshop on Spallation Materials Technology.

[23] S.A.H. Feghhi, Z. Gholamzadeh, C. Tenreiro, Investigation of the optimal material type and dimension for spallation targets using simulation methods, J. Theor. Appl. Phys. 8 (1) (2014) 117.

[24] T. Brückel, T. Gutberlet, et al., Conceptional Design Report JÜlich High Brilliance Neutron Source, Vol. 8, J-HBS, Forschungszentrum Jülich, 2020.

[25] L.J. Cox, S.D. Matthews, MCNP6™ Release 1.0: Creating and Testing the Code Distribution, Tech. Rep. LA-UR-13-24008, Los Alamos National Laboratory, Los Alamos, NM, USA, 2013.

[26] M. Chadwick, M. Herman, P. Obložinský, M. Dunn, Y. Danon, A. Kahler, D. Smith, B. Pritychenko, G. Arbanas, R. Arcilla, R. Brewer, D. Brown, R. Capote, A. Carlson, Y. Cho, H. Derrien, K. Guber, G. Hale, S. Hoblit, S. Holloway, T. Johnson, T. Kawano, B. Kiedrowski, H. Kim, S. Kunieda, N. Larson, L. Leal, J. Lestone, R. Little, E. McCutchan, R. MacFarlane, M. MacInnes, C. Mattoon, R. McKnight, S. Mughabghab, G. Nobre, G. Palmiotti, A. Palumbo, M. Pigni, V. Pronyaev, R. Sayer, A. Sonzogni, N. Summers, P. Talou, I. Thompson, A. Trkov, R. Vogt, S. van der Marck, A. Wallner, M. White, D. Wiarda, P. Young, Endf/b-vii.1 nuclear data for science and technology: Cross sections, covariances, fission product yields and decay data, Nucl. Data Sheets 112 (12) (2011) 2887–2996, special Issue on ENDF/B-VII.1 Library.

[27] T. Rinckel, D. Baxter, J. Doskow, P. Sokol, T. Todd, Target performance at the low energy neutron source, Physics Procedia 26 (2012) 168–177, proceedings of the first two meetings of the Union of Compact Accelerator-Driven Neutron Sources.

[28] V. Astrelin, A. Burdakov, P. Bykov, I. Ivanov, A. Ivanov, Y. Jongen, S. Konstantinov, A. Kudryavtsev, K. Kuklin, K. Mekler, S. Polosatkin, V. Postupaev, A. Rovenskikh, S. Sinitskiy, E. Zubairov, Blistering of the selected materials irradiated by intense 200 keV proton beam, J. Nucl. Mater. 396 (1) (2010) 43–48.

[29] A. San-Martin, F.D. Manchester, The H-Ta (hydrogen-tantalum) system, J. Phase Equilib. 12 (3) (1991) 332–343.

[30] A. Koning, D. Rochman, J.-C. Sublet, N. Dzysiuk, M. Fleming, S. van der Marck, Tendl: Complete nuclear data library for innovative nuclear science and technology, Nucl. Data Sheets 155 (2019) 1–55, special Issue on Nuclear Reaction Data.

[31] J.F. Ziegler, M. Ziegler, J. Biersack, SRIM – The stopping and range of ions in matter (2010), Nucl. Instrum. Methods Phys. Res. B 268 (11) (2010) 1818–1823, 19th International Conference on Ion Beam Analysis.

[32] A. Ferrari, P.R. Sala, M., A. Fasso, J. Ranft, Fluka: A multi-particle transport code, 2005, http://dx.doi.org/10.2172/877507, URL https://www.osti.gov/biblio/877507.

[33] N. Ophoven, E. Mauerhofer, J. Li, U. Rücker, P. Zakalek, J. Baggemann, C.L. Thomas Gutberlet, Thomas Brückel, Monte Carlo simulation of proton- and neutron-induced radiation damage in a tantalum target irradiated by 70 MeV protons, Appl. Phys. A 127 (2021).

[34] Q. Ding, Theoretical optimization and experimental validation of a microchannel target for a high-current accelerator-driven neutron source, dissertation, in: Rheinisch-Westfälische Technische Hochschule Aachen, Aachen, veröffentlicht auf dem Publikationsserver der RWTH Aachen University; Dissertation, Rheinisch-Westfälische Technische Hochschule Aachen, 2023, 2023.

[35] F. Cardarelli, Materials Handbook, Springer International Publishing, 2008.

[36] B. Agostini, M. Fabbri, J.E. Park, L. Wojtan, J.R. Thome, B. Michel, State of the art of high heat flux cooling technologies, Heat Transf. Eng. 28 (4) (2007) 258–281.

[37] P. Mastinu, J. Praena, G. Martìn-Hernàndez, N. Dzysiuk, G. Prete, R. Capote, M. Pignatari, A. Ventura, Status of the LEgnaro NeutrOn Source facility (LENOS), Physics Procedia 26 (2012) 261–273, proceedings of the first two meetings of the Union of Compact Accelerator-Driven Neutron Sources.

[38] R. Knight, D. Hall, J. Goodling, R. Jaeger, Heat sink optimization with application to microchannels, IEEE Trans. Compon. Hybrids Manuf. Technol. 15 (5) (1992) 832–842.

[39] J. Lackmann, H. Mertens, K.-H.G.W. Beutz, Dubbel: C Festigkeitslehre, Vol. 19, Springer, Berlin, Heidelberg, New York, 1997.

[40] FKM, Rechnerischer Festigkeitsnachweis FÜr Maschinenbauteile, Forschungskuratorium Maschinenbau, Frankfurt Main, Germany, 2012.

[41] W. Wagner, et al., The IAPWS industrial formulation 1997 for the thermodynamic properties of water and steam, ASME J. Eng. Gas Turbines Power 122 (2000) 150–185.

[42] A. Schmidt, T. Hirai, S. Keusemann, M. Rödig, G. Pintsuk, J. Linke, H. Maier, V. Riccardo, G.F. Matthews, M. Hill, H. Altmann, First demonstration of non-destructive tests on tungsten-coated JET divertor CFC tiles in the electron beam facility JUDITH-2, Phys. Scr. 2009 (T138) (2009) 014034.